ADVANCED OPTICAL MATERIALS
www.advopticalmat.de

A Narrowband Photo-Thermoelectric Detector Using Photonic Crystal

*Hosein Monshat, Longju Liu, and Meng Lu**

Here, a wavelength-specific photo-thermoelectric (PTE) device is reported that achieves narrowband optical absorption and thermoelectric conversion functions using a stack of thin films on a grating-patterned substrate. Conventional PTE devices are broadband with the absorption of electromagnetic radiation from ultraviolet to terahertz. There are demands for PTE devices that can exhibit narrowband response at a desired wavelength. Here, the narrowband PTE device consists of a photonic crystal (PC) filter with metal cladding and a thin-film thermocouple. The PC-PTE design is investigated numerically to illustrate the underlying energy conversion mechanism. The device is fabricated using nanoreplica molding followed by coating of thin films. The fabricated metal-cladding PC resonator exhibits a narrowband optical absorption with a resonant absorption coefficient of 85.4% and full-width-half-maximum of 14.8 nm in the visible wavelength range. The PTE measurements show that the thermoelectric output is sensitive to the coupling of incident light and guided-mode resonance modes. Illuminated under the resonant condition, the PTE device exhibits a responsivity and noise equivalent power of 0.26 V W^{-1} and 7.5 nW $Hz^{-1/2}$, respectively. This PC-PTE technology has the unique attributes of narrowband detection, large surface area, and low cost for the potential application in sensors, optical spectroscopy, and imaging.

1. Introduction

Photo-thermoelectric effect (PTE) represents a light-induced photocurrent generated by a thermoelectric material or a thermocouple junction.[1–3] A PTE device can absorb electromagnetic radiation, convert the absorbed energy into heat, and raise the device temperature. The temperature rise subsequently creates an electrical current flow, whose amplitude depends on the Seebeck coefficients of the thermoelectric materials. Different types of PTE-based detectors have been developed to measure light in a broad spectral range from visible to terahertz.[4–8] Applications of the PTE device include characterization of thermal transport properties of materials, wide temperature range measurements, spin-polarized power sources, energy harvesting, measuring dynamic thermal parameters of solid samples (photothermal calorimetry), and infrared to terahertz detection.[5,9–12] In contrast to the broadband PTE devices, a narrowband PTE device is designed to be more sensitive to a specific wavelength and can be implemented to provide spectral information during an analysis.[9,13–15] To obtain a narrowband PTE device, one solution is to place a bandpass optical filter in front of a broadband PTE sensor.[16,17] In contrast, the integration of a PTE sensor and optical filter on the same chip will result in a compact and cost-effective design.

A variety of photonic devices has been demonstrated with narrowband optical responses owing to optical resonance. For example, the microring and microsphere resonators, distributed feedback resonator, photonic crystal structures, and plasmonic resonators have been extensively studied.[18–21] Among these optical resonators, photonic crystal (PC) slabs that support the guided-mode resonance are particularly interesting in terms of their capability of developing a wavelength specific PTE device. The PC structure, also called leaky-mode waveguide, consists of a subwavelength grating and dielectric waveguide. Because the grating structure can couple incident light into a resonant mode, the PC structure displays narrowband reflection or transmission in a broad wavelength range.[21,22] Adding a metal cladding to the grating waveguide, PC structure can also exhibit narrowband absorptions.[23] The resonance characteristics of a PC device are determined by the grating geometry, material properties, and coupling condition.[24–27] In addition, the PC structure can be fabricated inexpensively over a large surface area on different substrates such as glass and plastics.[28] These features are of practical importance for the development of a narrowband PTE device.

Here, we demonstrate a PC-PTE device for narrowband optical detections in the visible wavelength range. The PC-PTE device integrates a 1D guided-mode resonance grating and a gold–bismuth (Au–Bi) metal thermocouple. The gold thin-film layer functions as the metal cladding layer of the PC structure as well as the electrical conductor of the thermocouple junction. Owing to the resonance effect, the metal cladding PC resonator exhibits narrowband absorption at a specific wavelength. The device is fabricated inexpensively using nanoreplica molding

H. Monshat, Prof. M. Lu
Department of Mechanical Engineering
Iowa State University
2128 Coover Hall, Ames, IA 50011, USA
E-mail: menglu@iastate.edu
Dr. L. Liu, Prof. M. Lu
Department of Electrical and Computer Engineering
2128 Coover Hall, Ames, IA 50011, USA

DOI: 10.1002/adom.201801248

and deposition of thin films. The narrowband absorption features of the device are numerically studied and experimentally investigated. The key performances, including absorption band diagram, thermal electrical voltage spectrum, device responsitivity, noise equivalent power, and input–output relationship are measured and reported.

2. Results and Discussion

2.1. Design and Fabrication of the PC-PTE Structure

Structure of the PTE device is schematically shown in **Figure 1**a. The device was fabricated on a 200 µm thick plastic substrate with the surface area of 1 cm^2. The PTE junction is located at the center and consists of a stack of the PC grating and a metal thermocouple. The shape of the junction is a dot with a radius of 1.4 mm. Au and Bi were chosen to form the thermocouple. The difference between the Seebeck coefficients of Au (S_{Au} = 6.5 µV K^{-1}) and Bi (S_{Bi} = −72 µV K^{-1}) was utilized to convert the light-induced local temperature rise to and a voltage output. The 0.6 mm wide and 10 mm long metal wires (Figure 1a) connect the junction to the contact pads. Lowering thermal mass of the junction area is the key point in decreasing device response time. Figure 1b illustrates the cross-section view of the junction consisting of a 1D PC and a Au/Bi thermocouple. The grating stack, including a period (Λ), grating height (h), and waveguide thickness (t_{TiO_2}) can be designed to achieve a guided-mode resonance at the desired wavelength. For our design, the grating geometries are Λ = 365 nm, duty cycle = 50%, h = 50 nm, and t_{TiO_2} = 100 nm. The device was fabricated on a plastic film using nanoimprint lithography. Details of the fabrication process are described in the Experimental Section.

Figure 1c shows the scanning electron microscopy (SEM) image of a cross section of the fabricated device. The Au layer resides between the TiO_2 and Bi films and serves simultaneously as the metal cladding of the TiO_2 grating waveguide and one metal side of the thermocouple. Due to the material loss of the Au layer at the guided-mode resonance wavelength (λ_r), the light will be coupled into the resonance and absorbed strongly. In contrast, the off-resonance wavelengths will be reflected instead of absorbed. As a result, the reflection and absorption spectra exhibit a dip and peak at λ_r, respectively. The thermocouple formed at the interface of the Au (t_{Au} = 150 nm) and Bi (t_{Bi} = 150 nm) layers can measure the local temperature rise caused by the narrowband absorption around λ_r.

2.2. Numerical Characterization of the PC-PTE Device

The optical phenomena of the metal-cladding PTE device are modeled using the finite-difference time-domain (FDTD) simulation and the numerical results are summarized in **Figure 2**. The calculated absorption spectra of the TE and TM mode are compared in Figure 2a. For the TE mode, there is a resonance peak at $\lambda_{r,TE}$ = 635 nm with a full-width half-maximum (FWHM) of 20.1 nm. The TM mode is associated with the

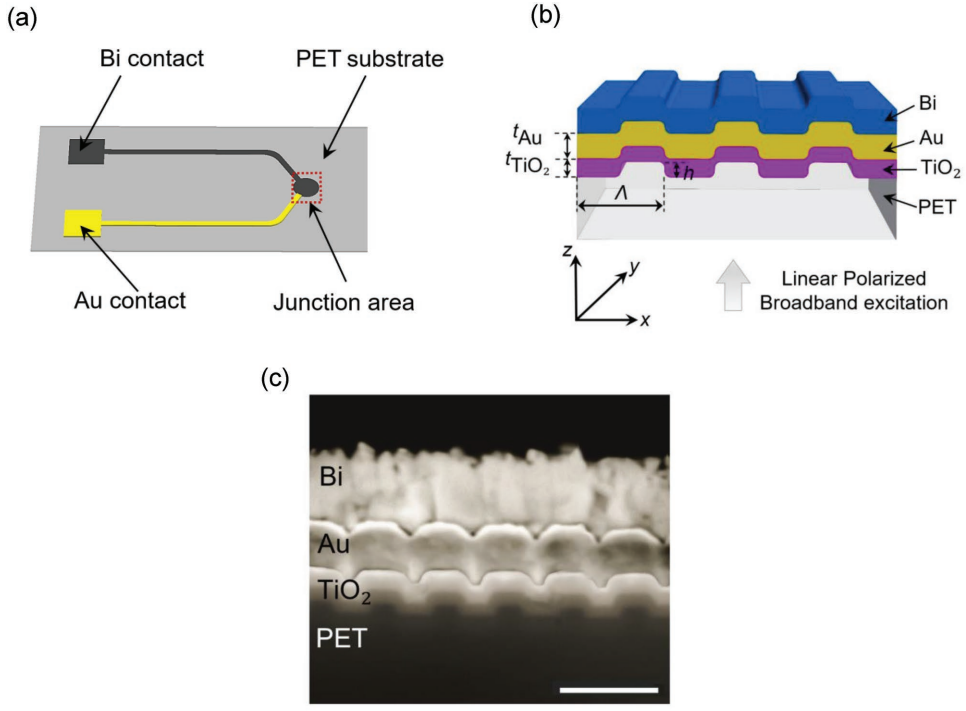

Figure 1. Structure of the PC-PTE device. a) Schematic plot of a narrowband PTE device on a plastic substrate. The junction area consists of the PC grating and Au/Bi thermocouple. The Au and Bi contact pads are placed sufficiently far from the junction to function as the reference temperature. b) Schematic illustration of the PC-PTE device from a cross-sectional view. The excitation illuminates the device through the plastic substrate. c) Cross-sectional SEM image of the junction area showing the grating and thin-film stack of TiO_2/Au/Bi layers. Scale bar, 500 nm.

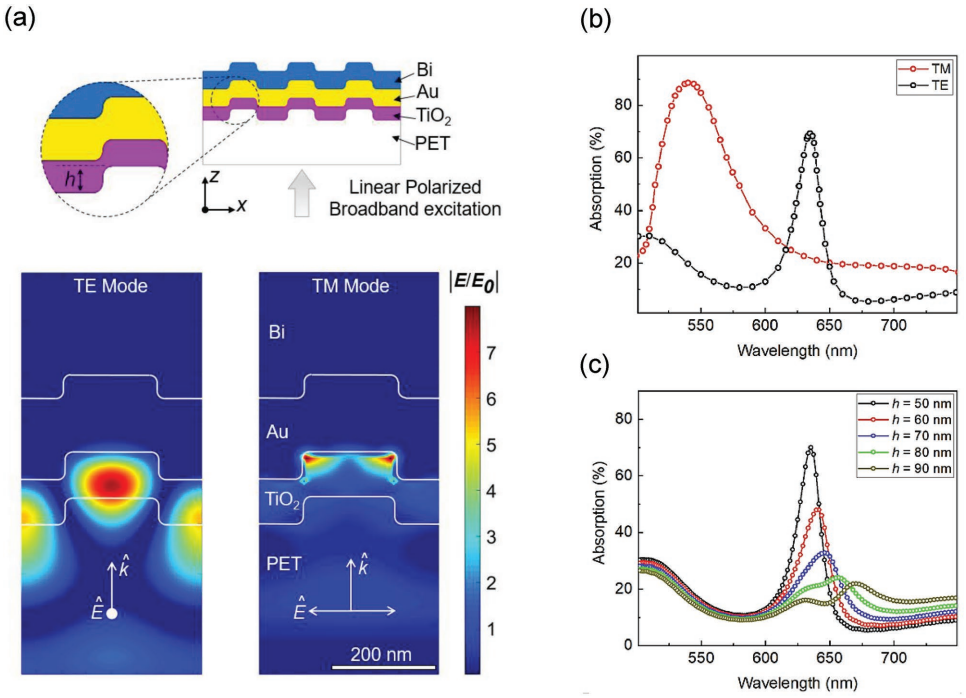

Figure 2. FDTD simulation of absorption resonances in the metal-cladding PC structure. a) Distributions of the local electrical fields $E(x, z)$ within one period of the device. For the TE (left panel) and TM (right panel) modes, the fields are shown at the resonant wavelengths of $\lambda_{r,\,TE} = 635$ nm and $\lambda_{r,\,TM} = 540$ nm, respectively. b) Absorption spectra for the TE (black) and TM (red) modes. c) Absorption spectra for a PC-PTE device with the grating height ranging from $h = 50$ to 80 nm.

surface plasmon resonance at the Au/TiO_2 interface and the TM absorption peak locates at $\lambda_{r,TM} = 540$ nm with a FWHM of 60.2 nm. Compared to the TM mode, the TE mode offers a narrower bandwidth for the wavelength-selective absorption. The FWHM of the TE mode is strongly dependent on the grating height. Figure 2b shows the absorption spectra of the PC gratings with different grating heights of $h = 50$, 60, 70, 80, and 90 nm. The increase of the grating height significantly broadens the resonance linewidth from 20.1 to 57.2 nm. Meanwhile, the peak of the absorption resonance exhibits a redshift and the absorption coefficient decreases from 70.3% to 22.1%. To further understand the interaction of light and the PC device, we calculated the distributions of electromagnetic field near the device surface when the device was excited at the resonance conditions. As shown in Figure 2c, for the TE mode, the electric field is confined inside the TiO_2 waveguide layer with a field enhancement factor of $|E/E_{inc}| = 8$. In contrast, the TM mode resides at the interface of the Au and TiO_2 layers. The spatially concentrated electromagnetic field will facilitate the heat generation at the thermoelectric junction of Bi and Au layers.

The absorbed photon energy causes heat generation and locally raises the temperature at the Bi/Au junction. The thermodynamic process near the PC-PTE device was simulated using finite element method (FEM). The details of the FEM analysis are given in the Experimental Section. **Figure 3**a shows the temperature distribution around the device when the device is illuminated by a TE-polarized beam at $\lambda_r = 635$ nm and $P = 400$ μW. Assuming the absorption coefficient of 75%, the heat source of 300 μW was placed underneath the Bi/Au junction. With the ambient temperature of 20 °C, the junction temperature increases 20.7 °C. Figure 3a also shows a higher heat flux toward the Au strip rather than the Bi side due to the higher thermal conductivity of Au compared to Bi. The dynamic change of temperature was calculated when the device was under a constant illumination of 400 μW. It takes up to 60 s for the temperature to reach the steady state temperature of 20.7 °C. The rise time when the device temperature reaches to the 60% of its final temperature is $\tau = 5.1$ s. As demonstrated in Figure 3b, decreasing the plastic thickness from 0.2 to 0.025 mm reduces the rise time from 5.1 to 1 s respectively. Decreasing the plastic thickness also elevates ΔT about 40% due to lower thermal mass.

2.3. Optical Characterization of the Narrowband PTE Device

The absorption signature of the metal cladding PC shows a strong dependency on the wavelength and incident angle of the excitation light. The dispersion diagram of the device was measured using the optical setup illustrated in **Figure 4**a. The sample was illuminated using a linearly polarized broadband light and the reflection spectra ($R(\lambda)$) were captured using a spectrometer. Because the gold film is sufficiently thick, there was no transmission ($T(\lambda) = 0$) through the device, thus the absorption spectra were calculated as $A(\lambda) = 1 - R(\lambda)$. Figure 4b represents the absorption dispersion diagram of the metal cladding PC structure shown in Figure 1c. The incident angle and wavelength range from 0° to 15° and 375 to 1025 nm, respectively. Two continuous bands can be identified across the visible

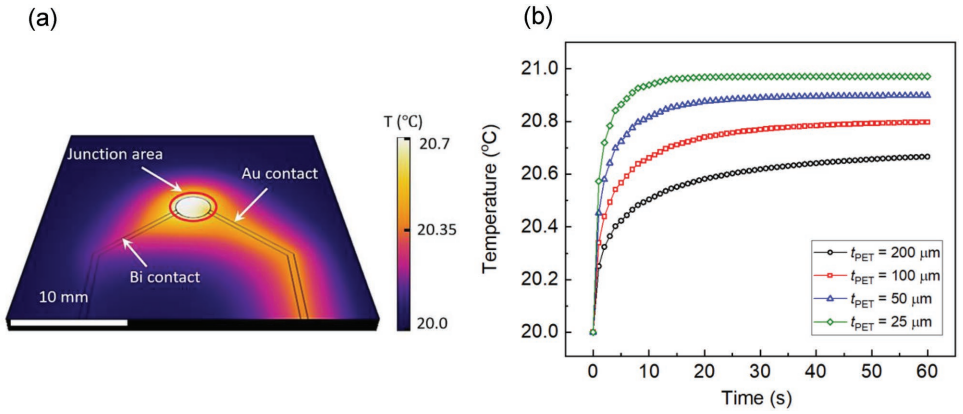

Figure 3. Heat transport simulation of PC-PTE device. a) Temperature distribution around the Au/Bi thermocouple when the device is optically heated to its saturation temperature. The boundary heat source with the input power of 360 μW is imposed on the junction area highlighted by the red circle. The thickness of the plastic substrate is 200 μm. b) Dynamic temperature responses as a function of time for PTE device with different substrate thickness. The response time is when the temperature reaches 60% of the saturation temperature. The response times of 5.1, 2.7, 1.7, and 1 s for PET thicknesses of 200, 100, 50, and 25 μm were calculated, respectively.

range. The experimental result shows an adequate agreement with the simulation results. For instance, at $\theta_i = 0°$, the device exhibits an absorption peak at $\lambda_r = 623$ nm with the FWHM of 29.2 nm. As illustrated in Figure 4c, to obtain an absorption resonance at 655 nm, the angle of incidence should be tuned to $\theta_i = 5°$ where the resonance peak at $\theta_i = 0°$ splits into two resonances at 655 nm ($A = 78.2\%$ and FWHM = 14.8 nm) and 588 nm ($A = 85.4\%$ and FWHM = 26.2 nm). The upper and lower absorption bands show the dispersion rates of 6.8 and −6.6 nm deg^{-1}, respectively.

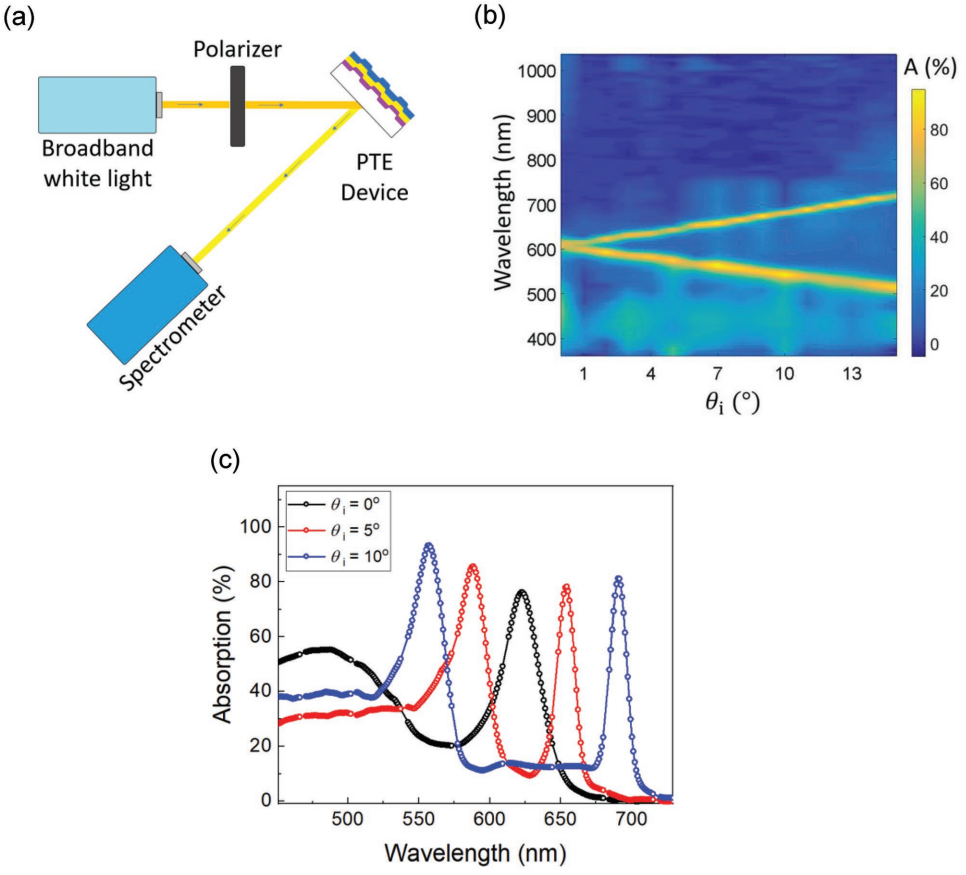

Figure 4. Measured absorption characteristics of the device. a) Schematic diagram of the optical setup used to measure the sample absorptions. b) Dispersion diagram of the TE-polarized absorbance. The upper and lower bands and lower band merges at $\theta_i = 0°$. c) Absorption spectra of metal-cladding PC device measured at three different angle incidences ($\theta_i = 0°$, 5°, and 10°).

2.4. Characterization of the PC-PTE Detector

2.4.1. Measurement of Thermoelectric Voltage

Thermoelectric voltage (TEV) output of the PC-PTE device depends on the intensity, polarization, wavelength, and angle of incidence of the excitation light. To characterize the PTE effect, we measured the TEV signals of the PC-PTE device illuminated by a wavelength tunable or angle tunable monochromatic light. As shown in **Figure 5**a, the broadband emission from a Xenon arc lamp is filtered using a grating-based monochromator and a polarizer to obtain the TE-polarized excitation at the desired wavelength. Outputs of the PTE device were recorded while the monochromatic light illuminated the PTE device under different conditions. Figure 5b plots the TEV output as a function of wavelength in case of normal incidence ($\theta_i = 0°$). The peak of the TEV spectrum is observed at $\lambda_r = 617$ nm ($P = 43$ μW mm^{-2}) with an output voltage of 60 μV which represents a temperature rise of ≈0.8 °C.

The angle-dependent output was analyzed by measuring TEV signal when the angle of incidence was tuned from 2° to 20° and the wavelength was kept at 660 nm. To facilitate the measurement, a 660 nm diode laser with an output power of $P = 300$ μW was used as the excitation. According to the absorption diagram shown in Figure 4b, at 660 nm, the absorption peak locates at 7.5°. The measured TEV voltage versus θ_i is shown in Figure 5c. The peak of TEV output presents at $\theta_i = 7.5°$, which is in an agreement with the absorption measurement. The results of TEV measurements show a clear correlation of the absorption and the TEV signal. Thus, the PC-PTE device can be exploited to detect light at a specific wavelength by tuning the angle of incidence and vice versa.

2.4.2. Responsivity and Noises

The responsivity of the PTE device can be obtained by normalizing the TEV spectrum to the incident power ($P(\lambda)$). Here, we calculated responsivity curves at three different angles of incidence ($\theta_i = 0°$, 5°, and 10°) as shown in **Figure 6**a. For the normal incidence case, the responsivity curve shows the narrowband feature at $\lambda_r = 617$ nm with a FWHM of 30.5 nm. Increasing the angle of incidence results in the splitting of the peak toward a longer and shorter wavelength. When $\theta_i = 5°$,

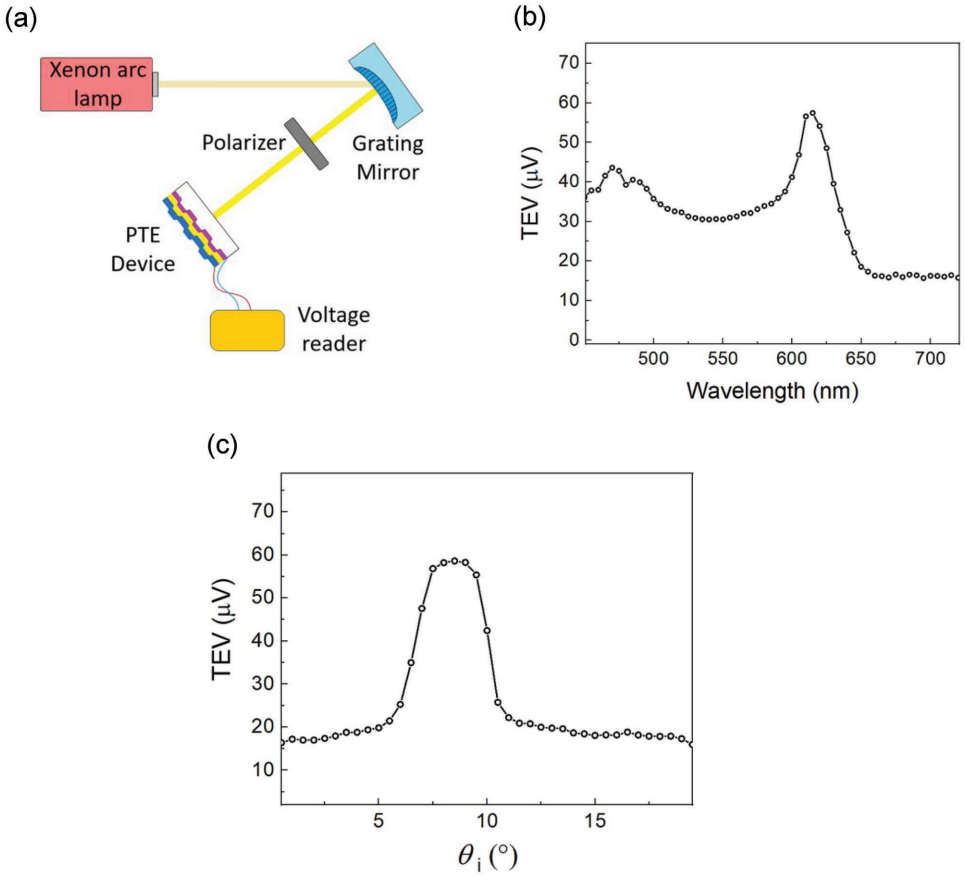

Figure 5. Characterization of TEV outputs of the PC-PTE device. a) Schematic diagram of the wavelength-dispersed TEV measurement. b) Measured TEV outputs as a function of wavelength when a TE-polarized monochromatic beam illuminated the device. The excitation beam was tuned in the wavelength range of 450 to 720 nm, with the power of $P = 300$ μW and $\theta_i = 0°$. c) Measured TEV versus angle of incidence. The excitation wavelength and power are $\lambda = 660$ nm and $P = 300$ μW, respectively.

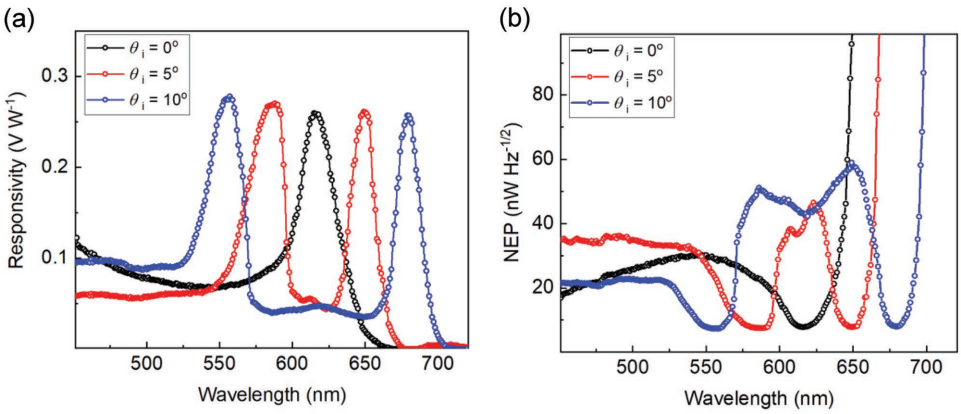

Figure 6. Noise analysis of the narrowband PTE detection. a) Responsivity spectra measured with angles of incidence of $\theta_i = 0°$, 5°, and 10°. b) NEP spectra calculated based on Johnson–Nyquist noise approximation.

two peaks appear at $\lambda_{r,b} = 587$ nm and $\lambda_{r,r} = 651$ nm. To further increase the θ_i to 10°, we can shift the peaks to $\lambda_{r,b} = 556$ nm and $\lambda_{r,r} = 680$ nm, respectively. The peaks in the responsivity curve match the absorption signatures shown in Figure 4c. The angle-dependent responsivity enables us to amplify the device output at a target wavelength by turning the angle of incidence.

Noise analysis was performed to evaluate the noise equivalent power (NEP) of the device. In our experiment, the Johnson–Nyquist noise is the dominant noise source. Therefore, the noise spectral density (NSD) can be calculated using $\mathrm{NSD} \approx \mathrm{NSD}_{\mathrm{Johnson}} = \sqrt{4Rk_BT}$, where R is the electrical resistance, k_B is the Boltzmann's constant, and T denotes the temperature. The resistance of our PTE device is about 260 Ω, whose change to temperature is negligible ≈1 μΩ. A Johnson noise of ≈2 nV Hz$^{-1/2}$ is calculated at room temperature, hence any noise density detection above that value is attributed to temperature rise. Furthermore, the NSD levels at the resonant wavelengths are below 7.5 nV Hz$^{-1/2}$. The noise equivalent power, which is equal to the NSD divided by responsivity, is shown in Figure 6b. The lowest NEP corresponds to a high detectivity $\left(\mathrm{D} = \frac{1}{\mathrm{NEP}} = \frac{\text{responsivity}}{\mathrm{NSD}}\right)$ of ≈130 MHz$^{1/2}$ W^{-1} at λ_r for normal and angled incident light owing to the low electrical resistance of the PTE device.

2.4.3. Dynamic Response

In Section 2.2, the dynamics of the heating process were modeled using the FEM simulation. To characterize the photothermal process, we recorded the device outputs dynamically when the excitation was turned on and off. The device was tested reactively under the on-resonance conditions. The device was illuminated from the normal direction using a monochromatic light at 623 nm with the power of 550 μW. The dynamic TEV outputs are shown in **Figure 7**a for two full cycles of optical heating and air cooling. The optical heating resulted in the TEV signal of 100 μV and the corresponding time for the PTE device to reach 60% of its final temperature or output voltage (response time) of $\tau = 3.9$ s. As discussed previously, the relatively large thermal mass of the device is limiting the temperature rise and time to reach thermodynamic equilibrium.

2.4.4. Input–Output Relation

Figure 7b illustrates the TEV output as a function of the incident power ranging from 50 to 550 μW. The excitation wavelength was $\lambda_i = 623$ nm and the coupling angles for the on-resonant cases were $\theta_i = 0°$. A linear relation between TEV

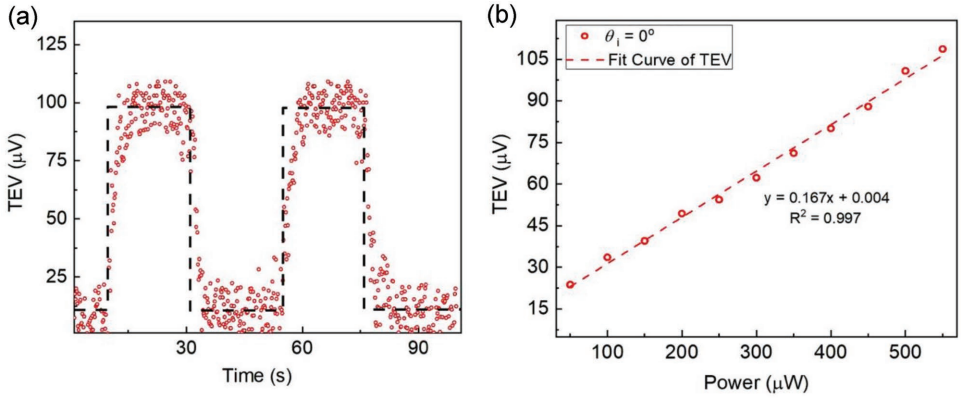

Figure 7. Dynamic TEV output measurement. a) The TEV outputs are plotted during two on and off cycles. The excitation light is TE-polarized with $\lambda_r = 660$ nm and $P = 550$ μW is modulated with the frequency of 50 mHz. b) Linear relationship between TEV outputs and TE-polarized light power with $\lambda_r = 660$ nm.

and incident power is observed. At incident power of 550 μW, a maximum TEV of 108.7 and 62.5 μV was measured. According to the linear fittings shown in Figure 7b, the on-resonance signal shows a slope of 0.167 V W^{-1}.

3. Conclusion and Discussion

We reported a narrowband PC-PTE device for the wavelength-specific detection of light. The device is based on the integration of a metal-cladding PC absorption filter and thin-film metal thermocouple. The PC filter with the Au cladding layer exhibited a narrowband absorption in the wavelength range of 500–750 nm with a FWHM of 15 nm. The light absorption can cause a temperate rise, and a consequent TEV output forms the Au/Bi thermocouple. The results show that the TEV signal is sensitive to the coupling of incident light and the guided-mode resonance modes. Illuminated under an on-resonance condition, the device shows the responsivity and NEP of 0.26 V W^{-1} and 7.5 nW $Hz^{-1/2}$, respectively. A linear relationship between incident light power and the output voltage has been observed with a slope of 0.167 V W^{-1}.

For future work, we plan to improve the performance of PC-PTE device from the following aspects. First, the substrate thickness will be reduced to eliminate the excessive thermal mass from the detector. The PC-PTE structure will be fabricated on a free-standing membrane. The low thermal mass will significantly reduce the response time and increase the equivalent temperature. Second, materials with a higher contrast of their Seebeck coefficients will be adopted to form the thermocouple. The compatible high Seebeck coefficients materials, such as Sb_2Te_3, Bi_2Te_3, and Ge, can increase the TEV output by a factor of six. Third, by engineering the grating structure, the bandwidth of the device can be future reduced and the device can also be designed to operate in the near-IR and middle wavelength IR ranges for applications in IR optics.

4. Experimental Section

Fabrication Process: The nanoreplica molding technique was used to fabricate the subwavelength grating on 200 μm polyethylene terephthalate (PET) substrate (Mylar Polyester Film, Grafix Plastics).[29] A silicon stamp carrying the reserve grating pattern was used as the mold. The silicon stamp itself was fabricated using the conventional electron beam lithography and reactive ion etching processes. To transfer the grating pattern from the silicon stamp, a drop of liquid ultraviolet curing adhesive (NOA-88, Norland Products) was dispensed and squeezed between the silicon stamp and the plastic substrate. The liquid adhesive was exposed to ultraviolet light at room temperature and polymerized. As a result, the desired grating pattern was formed at the surface of cured adhesive. After the curing, the plastic substrate was carefully separated from the replica. Next, the TiO_2 layer was deposited on top of the polymer grating using an electron beam evaporator (BJD-1800, Temescal). The thickness and refractive index of the TiO_2 layer were measured using an optical profilometer (F20, Filmetrics Inc.). To create the Au/Bi thermocouple, the Au and Bi conductors were deposited using the electron beam evaporation. The metal wires were coated through two acrylic shadow masks which were patterned using a laser cutter (ULTRA 9, Universal Laser Systems). Silver conductive epoxy (CW2400, CircuitWorks) was used to attach two metal wires to the Au and Bi contacts, respectively.

Numerical Modeling: The FDTD simulations were performed in two-dimensions using a software package (FDTD Solutions, Lumerical Inc.). The simulation domain was truncated to the one-unit volume of the periodic PC structure and periodic boundary conditions were imposed at the boundaries perpendicular to the *x*-axis. Perfectly matching layers were applied as the absorbing boundaries at the *z* and −*z* directions. The coordinator is defined in Figure 1b. The 1D PC grating with the metal cladding was illuminated with a plane wave propagating in the *z*-direction through the plastic substrate. The plane wave was polarized along the *x*-axis for the TM polarization and *y*-axis for the TE polarization. The optical properties, including the refractive index and extinction coefficient for Au, Bi, and TiO_2, were taken from pervious published data.[30,31] Monitors were placed below the PC structure to calculate the reflectance ($R(\lambda)$) and transmittance ($T(\lambda)$) in the wavelength range from 500 to 750 nm. The absorption spectra were calculated by $A(\lambda) = 1 - R(\lambda) - T(\lambda)$. The near-field distributions near the PC device were calculated at the resonant wavelength. The spatial distribution of the total electric field within one-unit cell was exported and plotted using MATLAB.

Temperature distribution profile through the PTE device was numerically calculated using a finite element-based simulation software (COMSOL Multiphysics 5.3).[32] The simulation domain was discretized using four-noded tetrahedral meshes. The boundary condition of constant room temperature (T = 20 °C) was applied at the lateral boundaries around the device. The open boundary, which implies the contact with surrounding air at room temperature, was chosen to terminate the simulation domain on the top and bottom sides of the device. The constant heat source of 300 μW was imposed to the junction area. A time-dependent solver was used to solve Poissons equation for heat transfer, $\frac{\partial^2 T}{\partial x^2}+\frac{\partial^2 T}{\partial y^2}+\frac{\partial^2 T}{\partial z^2}-\frac{\rho c_p}{k}+\frac{\partial T}{\partial t}+\frac{\dot{e}_{gen}}{k}=0$, where T represents the temperature value at each mesh node, $\dot{e}_{gen}$ is the rate of heat generation (W m^{-3}) at the heat source, k denotes the heat conductivity, ρ is the material density, and C_p is the specific heat capacity. Interfaces between two materials were treated using the equivalent conductivity, $K_s = \frac{2k_1 k_2}{k_1 k_2}$, where k_1 and k_2 denote the heat conductivities of the materials in contact, respectively. The heat conductivity, heat capacity at constant pressure, and density of the materials, including air, Au, Bi, TiO_2, and PET, were taken from the built-in material library of COMSOL. These material properties vary with temperature. At T = 20 °C, the heat conductivity of Au, Bi, TiO_2, and PET are k_{Au} = 314 W m^{-1} K^{-1}, k_{Bi} = 10.5 W m^{-1} K^{-1}, k_{TiO_2} = 7.4 W m^{-1} K^{-1}, and k_{PET} = 0.2 W m^{-1} K^{-1}. The heat capacity values of Au, Bi, TiO_2, and PET are 127, 120, 680, and 1250 J kg^{-1} K^{-1}. The temperature values at junction area central node were calculated and recorded every 0.1 s for the period of 60 s as shown in Figure 3b.

Absorption and Band Diagram Measurements: Absorption measurements were carried out using a home-built setup. The setup used a fiber-coupled broadband light source (LS-1, Ocean Optics, Inc.) as the excitation. The excitation was collimated using a fiber tip collimator (F240SMA, Thorlabs Inc.) and polarized using a linear polarizer. A multimode fiber collected sample reflections and analyzed using a spectrometer (USB2000, Ocean Optics). Because the Au/Bi metal films were sufficiently thick, the transmission through the metal cladding PC device was nearly zero. The absorption spectra were obtained by calculating $A(\lambda) = 1 - R(\lambda)$. The sample reflectance was calculated with regard to the reflection of a mirror which served as a reference sample. To adjust the angle of incidence, the sample was mounted on a rotation stage. The reflection spectra were collected by rotating the sample over a range of angles ($0° < \theta_i < 15°$) with the increment of 1°. The absorption spectra were calculated and plotted using MATLAB.

TEV Measurement Setup: The wavelength-dependent measurement was performed using a narrowband light generated by a monochromator (Model 272, McPherson). The monochromator was equipped with a Xenon arc lamp as the input light source and an 1800 g mm^{-1} grating concave mirror. The output from the exit slit of the monochromator was collimated using an achromatic lens (AC254-100-A-ML, Thorlabs Inc.) and

polarized using the linear polarizer. The monochromator can scan in the spectral range of 450 to 800 nm and output monochromatic light with a FWHM of 2 nm. During the measurement, the monochromator scanned at the speed of 10 nm min^{-1} to minimize the influence of slow response time. The device was placed in an environment-controlled chamber equipped with a thermoelectric temperature controller (AC-073, TE Technology, Inc.) to maintain the chamber temperature at 20 ± 0.025 °C. Chambers walls were totally opaque to eliminate the ambient light influence on device characterization. The device was attached to a kinetic mount which was placed on a rotation stage to precisely adjust the angle of incidence. TEV signals were recorded as a function of the wavelength of the excitation. For the angle-dependent test, the laser diode (85-RCA-400, Melles Griot) served as the excitation at 660 nm with the output power of 300 μW. The TEV signals were recorded when the angle of incidence was tuned in the range of 0° to 20° with the incremental of 0.5°. To measure the dynamic TEV output, an optical chopper (SR540, Stanford Research Systems) was placed between the laser and sample to modulate the excitation beam at 50 mHz. The output currents were measured using a picoammeter (Model 6487, Keithley). The TEV values were calculated by multiplexing the current output and the resistance (260 Ω) of the PTE device was calculated using the current output device.

Acknowledgements

This work was supported by the National Science Foundation under Award No. ECCS 16-53673 and the National Institute of Food and Agriculture under Award No. 2018-67021-27968. Any opinions, findings, and conclusions or recommendations expressed in this material are those of the authors and do not necessarily reflect the views of the National Science Foundation. L.L. acknowledges the Catron Foundation Graduate Fellowship for financial support. The authors declare no competing financial interests.

Conflict of Interest

The authors declare no conflict of interest.

Keywords

guided-mode resonance, narrowband filters, photonic crystals, photothermoelectric effect

Received: September 12, 2018
Revised: October 30, 2018
Published online:

[1] A. C. Boccara, D. Fournier, in *Principles and Perspective of Photothermal and Photoacoustic Phenomena*, Vol. *1* (Ed: A. Mandelis), Elsevier Scientific Publication Company, New York, USA **1992**, p. 270.
[2] D. Basko, *Science* **2011**, *334*, 610.
[3] J. Mort, D. M. Pai, *Photoconductivity and Related Phenomena*, Elsevier Scientific Publication Company, New York, USA **1976** p. 323.
[4] G. Bao, K. Huang, *J. Opt. Soc. Am. A* **2005**, *22*, 1408.
[5] X. Cai, A. B. Sushkov, R. J. Suess, M. M. Jadidi, G. S. Jenkins, L. O. Nyakiti, R. L. Myers-Ward, S. Li, J. Yan, D. K. Gaskill, T. E. Murphy, H. D. Drew, M. S. Fuhrer, *Nat. Nanotechnol.* **2014**, *9*, 814.
[6] X. D. Xu, N. M. Gabor, J. S. Alden, A. M. van der Zande, P. L. McEuen, *Nano Lett.* **2010**, *10*, 562.
[7] D. Dadarlat, P. R. N. Misse, A. Maignan, E. Guilmeau, M. Depriester, M. Kuriakose, A. H. Sahraoui, *Proc. SPIE* **2015**, *9258*, 92582R.
[8] F. Sizov, A. Rogalski, *Prog. Quantum Electron.* **2010**, *34*, 278.
[9] D. Dadarlat, M. Streza, R. C. Y. King, F. Roussel, M. Kuriakose, M. Depriester, E. Guilmeau, A. H. Sahraoui, *Meas. Sci. Technol.* **2014**, *25*, 015603.
[10] M. H. He, Y. J. Lin, C. M. Chiu, W. F. Yang, B. B. Zhang, D. Q. Yun, Y. N. Xie, Z. H. Lin, *Nano Energy* **2018**, *49*, 588.
[11] H. Taghinejad, M. Taghinejad, A. Tarasov, A. Hosseinnia, H. Moradinejad, A. Eftekhar, E. Vogel, A. Adibi, *Conf. Lasers Electro-Opt.* **2017**, SW4O-5.
[12] Y. Yan, Z. M. Liao, X. X. Ke, G. Van Tendeloo, Q. S. Wang, D. Sun, W. Yao, S. Y. Zhou, L. Zhang, H. C. Wu, D. P. Yu, *Nano Lett.* **2014**, *14*, 4389.
[13] K. W. Mauser, S. Kim, S. Mitrovic, D. Fleischman, R. Pala, K. C. Schwab, H. A. Atwater, *Nat. Nanotechnol.* **2017**, *12*, 770.
[14] X. Q. Deng, Y. X. Wang, Z. R. Zhao, Z. Q. Chen, J. L. Sun, *J. Phys. D: Appl. Phys.* **2016**, *49*, 425101.
[15] M. Kuriakose, M. Depriester, R. C. Y. King, F. Roussel, A. H. Sahraoui, *J. Appl. Phys.* **2013**, *113*, 044502.
[16] R. Magnusson, S. S. Wang, *Appl. Opt.* **1995**, *34*, 8106.
[17] M. R. Tibuleac S, *J. Opt. Soc. Am. A* **1997**, *14*, 1617.
[18] A. A. Erchak, D. J. Ripin, S. Fan, P. Rakich, J. D. Joannopoulos, E. P. Ippen, G. S. Petrich, L. A. Kolodziejski, *Appl. Phys. Lett.* **2001**, *78*, 563.
[19] S. H. Fan, J. D. Joannopoulos, *Phys. Rev. B* **2002**, *65*, 235112.
[20] A. K. Kodali, M. Schulmerich, J. Ip, G. Yen, B. T. Cunningham, R. Bhargava, *Anal. Chem.* **2010**, *82*, 5697.
[21] J. N. Liu, M. V. Schulmerich, R. Bhargava, B. T. Cunningham, *Opt. Express* **2011**, *19*, 24182.
[22] R. Magnusson, M. Shokooh-Saremi, *Opt. Express* **2007**, *15*, 10903.
[23] I. M. White, J. D. Suter, H. Oveys, X. D. Fan, T. L. Smith, J. Y. Zhang, B. J. Koch, M. A. Haase, *Opt. Express* **2007**, *15*, 646.
[24] R. Magnusson, D. Wawro, S. Zimmerman, Y. W. Ding, M. Shokooh-Saremi, K. J. Lee, D. Ussery, S. Kim, S. H. Song, *Proc. SPIE* **2010**, *7604*, 76040M.
[25] M. J. Uddin, T. Khaleque, R. Magnusson, *Opt. Express* **2014**, *22*, 12307.
[26] J. A. Giese, J. W. Yoon, B. R. Wenner, J. W. Allen, M. S. Allen, R. Magnusson, *Opt. Lett.* **2014**, *39*, 486.
[27] M. Shokooh-Saremi, R. Magnusson, *Opt. Express* **2008**, *16*, 18249.
[28] A. V. Kabashin, P. Evans, S. Pastkovsky, W. Hendren, G. A. Wurtz, R. Atkinson, R. Pollard, V. A. Podolskiy, A. V. Zayats, *Nat. Mater.* **2009**, *8*, 867.
[29] L. J. Liu, H. A. Khan, J. J. Li, A. C. Hillier, M. Lu, *Nanotechnology* **2016**, *27*, 295301.
[30] P. B. Johnson, Christy, R. W. , *Phys. Rev. B* **1972**, *6*, 4370.
[31] W. S. M. Werner, K. Glantschnig, C. Ambrosch-Draxl, *J. Phys. Chem. Ref. Data* **2009**, *38*, 1013.
[32] D. Mrugala, T. Riebeck, W. Lang, *COMSOL Conf.*, IMSAS, Bremen, Germany **2011**.